Effect of Channel Geometry on the Performance of an Electrostatic Precipitator: A Comparative Numerical Study

applied sciences

MDPI

Article

Effect of Channel Geometry on the Performance of an Electrostatic Precipitator: A Comparative Numerical Study

Halil Kilic [1,*], Gozde Konuk Ege [2], Ismail Temiz [1], Garip Genc [1], Ozge Akay Sefer [1] and Ahmet Sefer [3]

[1] Department of Mechatronics Engineering, Faculty of Technology, University of Marmara, Istanbul 34722, Türkiye
[2] Mechatronics Program, Gedik Vocational School, Istanbul Gedik University, Istanbul 34876, Türkiye
[3] Electrical and Computer Engineering (ECE) Program, Computer Electrical and Mathematical Science and Engineering (CEMSE) Division, King Abdullah University of Science and Technology (KAUST), Thuwal 23955, Saudi Arabia
* Correspondence: halil.kilic@marun.edu.tr

Abstract

This study presents a numerical investigation of the influence of channel geometry on electrohydrodynamic (EHD) processes governing particle transport in electrostatic precipitators (ESPs). A conventional rectangular channel is compared with concave configurations using a coupled multi-physics model that accounts for gas flow, electric field distribution, ion transport, and particle migration across a wide particle-size range. The results show that geometric modification significantly alters ion transport and charge distribution within the ESP channel. Compared with the rectangular configuration, the concave profile enhances ion penetration and particle charging, leading to improved collection efficiency across the entire particle-size range. The improvement is particularly pronounced near the minimum-efficiency region for submicron particles. Specifically, near 0.1 μm, the collection efficiency increases from approximately 30% in the rectangular channel to approximately 50% for the higher-contraction concave configuration, representing an improvement of nearly 20 percentage points. A comparison with a Venturi-like contraction further shows that abrupt geometric contraction produces localized space-charge accumulation and reduces the effective charging region. In contrast, smooth concave shaping promotes a more distributed electrostatic interaction region, resulting in improved particle collection performance.

Keywords: electrostatic precipitator; channel geometry; electrohydrodynamic flow; particle charging; collection efficiency

Academic Editor: Alberto Benato

Received: 31 March 2026
Revised: 25 April 2026
Accepted: 27 April 2026
Published: 29 April 2026

1. Introduction

Atmospheric particulate matter (PM) pollution is widely recognized as one of the most persistent environmental challenges worldwide and poses significant risks to public health [1]. Fine particles are sufficiently small to bypass the natural defense mechanisms of the human respiratory system, allowing them to reach deep regions of the lungs and, in some cases, enter the systemic circulation, thereby contributing to long-term cardiovascular and respiratory complications [2]. Numerous epidemiological studies have reported strong statistical associations between chronic exposure to fine particulate matter and increased incidence of cardiopulmonary diseases, hospital admissions, and premature mortality [2]. With the continued expansion of industrial activity in both developed and

developing regions, emissions from manufacturing and production processes remain a major contributor to ambient particulate pollution [3]. Consequently, the development of reliable and high-efficiency industrial particulate control technologies has become a critical engineering priority for environmental protection and occupational health.

Among industrial emission control technologies, electrostatic precipitators (ESPs) are widely applied for large-scale particulate removal because they can handle high gas flow rates while maintaining low pressure drop and high collection efficiency [4]. In many industrial applications, ESPs are used to remove fly ash and other particulate pollutants from flue gases; however, the fractional collection efficiency of conventional ESPs can decrease in the submicron range, particularly for particles smaller than approximately 1 μm, motivating continued efforts to improve fine-particle control [4]. The fundamental physical principles of electrostatic precipitation were comprehensively established by Parker [5] and White [6], who showed that properly designed ESP systems can achieve collection efficiencies exceeding 90% under suitable operating conditions.

In addition to electrical operating conditions, the performance of electrostatic precipitators is strongly influenced by the complex interactions between the flow field, electric field, and particle transport processes. These coupled phenomena involve ion generation through corona discharge, space charge transport, electrohydrodynamic flow effects, and particle charging mechanisms within the ESP channel [7–10]. Because of this multi-physics behavior, experimental investigations alone are often insufficient to fully characterize the internal processes governing particle migration and collection. Consequently, computational fluid dynamics (CFD)-based numerical modeling has become an important tool for analyzing ESP performance and improving system design. Previous numerical studies have demonstrated that coupled simulations that incorporate electrostatic fields, gas flow dynamics, and particle transport can provide valuable insights into particle trajectories, charging behavior, and collection efficiency in electrostatic precipitators [7–9]. For example, Kılıç et al. [11] developed a numerical model that simultaneously solved the gas flow, electrostatic field, and particle motion equations to evaluate particle transport and collection efficiency in a wire–plate ESP.

Previous numerical and experimental studies have highlighted the importance of coupled electrohydrodynamic flow and particle transport processes in determining the performance of electrostatic precipitators. Numerical investigations have shown that particle charging mechanisms and particle transport behavior significantly influence the overall collection efficiency of ESP systems, particularly for fine particles in the submicron range [12]. Computational fluid dynamics (CFD) models that incorporate electric field distributions, space charge effects, and particle trajectory calculations have therefore been widely employed to analyze particle migration and collection characteristics within ESP channels [13,14]. These studies indicate that particle motion within electrostatic precipitators is governed by the interplay among electrostatic forces, fluid flow structures, and particle inertia. In addition, electrohydrodynamic flow generated by corona discharge can modify local velocity fields and influence particle transport and deposition patterns within the collection region [15]. More recent numerical simulations have further demonstrated that the space charge carried by dust particles can distort the electric field distribution and consequently affect corona discharge characteristics and particle collection efficiency [16]. Experimental investigation of electrostatic precipitators is often costly and technically complex due to the strong coupling between electric field, gas flow, and particle dynamics; therefore, numerical simulation approaches are frequently preferred for analyzing ESP performance and internal particle transport mechanisms. In this context, Skodras et al. [17] developed a CFD-based model for a wire–plate electrostatic precipitator that simultaneously solved the coupled gas flow, particle dynamics, and electrostatic field equations to predict particle trajectories and collection performance within the ESP

channel. These findings collectively emphasize that reliable ESP modeling requires a coupled analysis of electric field behavior, flow dynamics, and particle charging mechanisms.

Geometric configuration is widely recognized as a key design parameter influencing the performance of electrostatic precipitators (ESPs), as it directly affects the electric field distribution, internal flow structures, and particle transport behavior within the collection channel.

In recent years, various non-planar collecting plate geometries have been proposed to enhance ESP performance, including corrugated, wavy, and W-shaped structures. These configurations primarily aim to improve particle charging and collection efficiency by modifying the electrostatic field distribution, electrohydrodynamic (EHD) flow, and particle transport processes. For instance, corrugated plate geometries have been shown to significantly influence the electric field distribution, space charge density, and EHD flow structures, leading to improved particle capture performance [18,19]. Similarly, wavy collecting plates introduce periodic variations in curvature, where parameters such as amplitude and wavelength affect particle charging and transport behavior [20]. W-shaped plate configurations have also been proposed as an effective approach to for enhance fine particle collection, particularly in two-stage ESP systems, by combining a favorable electric field distribution with flow redirection and inertial effects [21].

In addition to these designs, conical collector geometries have been investigated, in which parameters such as cone inclination, flow velocity, and applied voltage are optimized to improve particle trajectories and collection efficiency [22]. However, these approaches primarily focus on performance-oriented parameter tuning and provide limited insight into the mechanistic role of geometry in modulating ion transport and EHD coupling.

Despite these advancements, existing designs are fundamentally based on oscillatory or segmented geometries with multiple curvature extrema, where performance improvements are predominantly associated with localized variations in flow and electric field characteristics. While previous studies demonstrate that geometric modifications can alter electrohydrodynamic (EHD) flow structures, space charge distribution, and particle dynamics, these effects are typically interpreted in terms of global performance metrics rather than through a detailed examination of the underlying transport mechanisms.

This gap in the literature is closely related to the inherent complexity of electrostatic precipitation, where gas flow, electric field, ion transport, and particle dynamics are strongly coupled [23]. Classical ESP formulations describe particle charging and migration primarily via ion attachment and Coulomb-driven motion in an electric field [24], while modern numerical studies emphasize the importance of multi-physics coupling, including EHD flow and space charge effects [25]. However, in most studies, ion transport is predominantly modeled as drift-dominated, and the role of convective transport is often considered secondary. In regions of a relatively weak electric field, ion drift velocity may become comparable to the gas velocity [23], suggesting that convective transport can influence space charge distribution and particle charging behavior. These observations indicate that the interaction between channel geometry and ion convective transport, and its role in modulating EHD coupling, has not yet been systematically analyzed.

In this context, the present study introduces an elliptical concave channel geometry characterized by a smooth, monotonic variation in curvature enabling a fundamentally different design paradigm based on continuous flow control rather than oscillatory modulation. Unlike conventional corrugated, wavy, W-shaped, and conical geometries, the proposed configuration enables a more stable and systematic regulation of EHD interactions between the flow field and electric field. The contraction ratio is introduced as a key design parameter, providing a quantitative framework for controlling flow–field coupling. Furthermore, the coupled interaction between the flow field and electric field is analyzed to demonstrate how EHD effects can enhance particle charging and transport behavior. From an engineering perspective, the proposed geometry offers a simple and

continuous structural modification with low retrofit complexity, making it suitable for practical industrial ESP applications.

2. Materials and Methods

2.1. Geometry Definition

The electrostatic precipitator (ESP) examined consists of two different configurations: a rectangular reference channel with a constant cross-section and a concave channel defined by elliptical arcs. The concave geometry is compared with the conventional rectangular channel, widely studied in the literature, to quantitatively investigate the effects of geometry on the electric field distribution and particle transport. The overall geometry of the model is schematically shown in Figure 1. The model is defined in a two-dimensional (2D) Cartesian coordinate system representing the longitudinal section of the channel; the x-axis denotes the flow direction, and the y-axis represents the channel height. Since the wire electrodes extend uniformly along the spanwise direction and the collecting plates are planar, the flow and electric field variations in the out of plane direction are assumed to be negligible. Therefore, a two-dimensional representation is sufficient to capture the dominant electrodynamic and particle transport mechanisms.

All geometries were created in the COMSOL Multiphysics 6.2 environment and configured for multi-physics solutions. The model is defined to solve the electrostatic fields, space-charge transport, laminar flow, and particle tracking physics in a coupled manner. This approach allows consistent and comparable evaluation of geometry-dependent field variations.

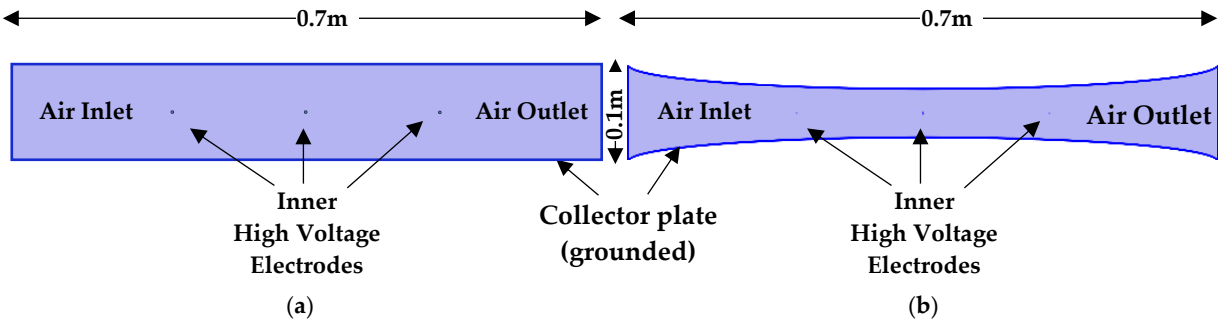

Figure 1. Rectangular and concave channel geometries with electrode configurations used in the electrostatic precipitator: (**a**) rectangular channel and (**b**) concave channel.

Both channel geometries have the same total channel length, which is defined as $L = 0.70$ m in the rectangular configuration; the channel height remains constant along the flow direction, whereas in the concave configuration, the channel cross-section exhibits a symmetric contraction–expansion profile with respect to the channel centerline. The reference rectangular geometry was chosen to represent a conventional wire–plate ESP configuration widely employed in numerical and experimental studies [26]. In the reference rectangular geometry, the channel half-height is defined as $h_0 = 0.05$ m (corresponding to a total channel height of $H_0 = 0.10$ m). The upper and lower walls of the concave channel are defined by elliptical arcs that are symmetric about the channel midpoint. The local half-height of the channel is expressed by the following function:

$$f(x) = h_0 - (h_0 - b_{min})\sqrt{1 - \left(\frac{2x-L}{L}\right)^2},\ 0 \le x \le \quad (1)$$

where $f(x)$ represents the local half-height of the channel along the flow direction and b_{min} denotes the minimum half-height at the channel center. According to Equation (1), the channel opening at the inlet and outlet sections remains equal to the reference value h_0, while the minimum opening occurs at $x = L/2$.

The local total channel height is therefore given by

$$H(x) = 2f(x). \quad (2)$$

The concavity level is defined by the dimensionless contraction ratio ε, which is expressed as

$$\varepsilon = \frac{h_0 - b_{min}}{h_0}. \quad (3)$$

In the parametric analysis, $\varepsilon = 0.25$ and $\varepsilon = 0.50$ were considered, corresponding to minimum half-height values of b_{min} = 0.0375 m and b_{min} = 0.025 m, respectively. Three wire electrodes with a radius of 0.5 mm are positioned along the channel centerline and supplied with a constant voltage of 20 kV. The upper and lower collecting plates are electrically grounded. All geometric and operating parameters used in the simulations are summarized in Table 1 to ensure model reproducibility.

Table 1. Geometric and operating parameters used in the simulations.

Parameter	Symbol	Value	Description
Channel length	L	0.70 m	Total channel length
Reference total height	H_0	0.10 m	Rectangular channel height
Reference half-height	h_0	0.05 m	Half channel height
Contraction ratio	ε	$0, 0.25, 0.50$	Dimensionless concavity parameter
Minimum half-height	b_{min}	$h_0(1-\varepsilon)$	Minimum channel opening at the concave center
Electrode radius	r_i	5×10^{-4} m	Wire electrode radius
Electrode spacing	s	0.15 m	Wire–wire distance
Applied voltage	V_0	20 kV	Applied high voltage
Inlet velocity	u_0	1 m/s	Uniform inlet flow velocity
Pressure	p	101,325 Pa	Ambient pressure
Temperature	T	293.15 K	Ambient temperature

2.2. Governing Equations

The multi-physics processes inside the electrostatic precipitator are investigated using a coupled numerical framework that simultaneously accounts for gas flow, electrostatic field, space-charge transport, and particle dynamics.

The flow field is solved to evaluate the influence of channel geometry on the electric-field distribution, space-charge transport, and particle migration within the precipitator. This approach enables the effect of geometric variation on the overall ESP performance to be assessed while minimizing the influence of additional modeling parameters.

The gas phase is assumed to behave as an incompressible Newtonian fluid. The flow field is governed by the steady-state Navier–Stokes and continuity equations, expressed as

$$\rho(\vec{u} \cdot \nabla)\vec{u} = -\nabla p + \mu\nabla^2\vec{u} + \rho_q\vec{E}, \quad (4)$$

$$\nabla.\vec{u} = 0, \quad (5)$$

where $\vec{u}$ represents the velocity vector, p denotes the pressure, ρ is the fluid density, and μ is the dynamic viscosity. The term $\rho_q \vec{E}$ represents the electrohydrodynamic body force generated by the interaction between the electric field and the space charge:

$$\vec{F}_{EHD} = \rho_q\vec{E}, \quad (6)$$

where $\vec{E}$ is the electric field vector and ρ_q denotes the space-charge density (C/m^3).

Under electrostatic conditions, the electric field is governed by Gauss's law together with the electric potential formulation. The differential form of Gauss's law and the relation between the electric field and the electric potential are written as

$$\nabla.\vec{E} = \frac{\rho_q}{\varepsilon_0}, \tag{7}$$

$$\vec{\mathrm{E}} = -\nabla \mathrm{V}. \tag{8}$$

Substituting Equation (8) into Equation (7) yields the Poisson equation for the electric potential, defined as

$$\nabla^2.\mathrm{V} = -\frac{\rho_q}{\varepsilon_0}, \tag{9}$$

where ε_0 represents the permittivity of free space (8.854×10^{-12} F/m), and V is the electric potential. Since corona discharge generates a non-zero space-charge density within the precipitator, the electrostatic field is described by the Poisson equation rather than the Laplace equation [27,28].

The transport of space charge within the domain is described by the charge conservation equation and the current density formulation:

$$\nabla.\vec{J} = 0, \tag{10}$$

indicating that no net charge accumulation occurs within the domain. Charge transport takes place through drift under the electric field and convection with the flow. Accordingly, the current density takes the form

$$\vec{J} = z_q \mu_i \rho_q \vec{E} + \rho_q \vec{u}, \tag{11}$$

where $\vec{J}$ is the current density vector (A/m^2), z_q is the ion charge number, and μ_i denotes the ion mobility. The first term represents the drift of ions along the electric field, whereas the second term corresponds to the convective transport of charge by the flow. Note that diffusion effects were neglected in Equation (11) as ion drift under strong electric field dominates the charge transport mechanism. This formulation is based on the classical space charge transport model widely used in corona discharge electrostatic precipitators [5,26].

Particle motion was simulated using a Lagrangian particle tracking approach. In this framework, individual particles are tracked by solving Newton's second law of motion under the influence of the surrounding flow and electric fields [26]. The particle position and velocity are governed by

$$\frac{d\vec{x}_p}{dt} = \vec{v}_p, \tag{12}$$

$$m_p \frac{d\vec{v}_p}{dt} = \vec{F}_t, \tag{13}$$

where $\vec{x}_p$ and $\vec{v}_p$ denote the particle position and velocity vectors, m_p is the particle mass, and $\vec{F}_t$ represents the total force acting on the particle.

In the present model, particle motion is governed primarily by the drag force and the electrostatic force. The particle–fluid interaction is described using the Cunningham–Millikan–Davis drag formulation, which accounts for rarefaction effects that become important for small particle diameters. The drag force acting on a particle is given by

$$\vec{F}_D = \frac{m_p}{\tau_p S}\left(\vec{u} - \vec{v}_p\right), \tag{14}$$

where $\vec{u}$ is the local fluid velocity, S is the Cunningham slip correction factor, and τ_p denotes the particle velocity response time, defined as

$$\tau_p = \frac{4\rho_p d_p^2}{3\mu C_d Re_p}. \quad (15)$$

Here, ρ_p and d_p are the particle density and diameter, respectively, and C_d is the drag coefficient. The particle Reynolds number is expressed as

$$Re_p = \frac{\rho|\vec{u}-\vec{v}_p|d_p}{\mu}, \quad (16)$$

where ρ and μ denote the fluid density and dynamic viscosity, respectively.

The Cunningham slip correction factor used in the drag formulation is given by

$$S = 1 + Kn\left(C_1 + C_2 e^{-C_3/Kn}\right), \quad (17)$$

where the Knudsen number Kn is defined as

$$Kn = \frac{\lambda}{d_p}, \quad (18)$$

with λ denoting the mean free path of the gas and d_p the particle diameter, while C_1, C_2, and C_3 are empirical constants associated with the Cunningham correction. Rarefaction effects were incorporated using the rarefaction correction option available in COMSOL Multiphysics. Charged particles are subjected to an electrostatic force under the electric field. The electrostatic force acting on the particle is given by

$$\vec{F}_e = q_p\vec{E} = eZ\vec{E}, \quad (19)$$

where q_p is the particle charge, e is the elementary charge, and Z is the dimensionless charge number of the particle [22,26].

The particle charging process was described using the classical Lawless charging model, which accounts for ion–particle interactions and the time-dependent accumulation of electric charge on particles in corona discharge environments [26]. Particles that reach the collecting plate surfaces are assumed to be captured.

2.3. Numerical Model and Boundary Conditions

The computational domain was discretized using an unstructured triangular mesh. A mesh independence study was performed to ensure that the numerical solution was not affected by the mesh-discretization level. For this purpose, three different mesh configurations, namely coarse, normal, and fine meshes, were systematically examined for all channel geometries. To visualize, Figure 2 shows the unstructured mesh levels for three different mesh configurations.

To quantitatively assess mesh convergence, the electric field magnitude distributions obtained with different mesh levels were compared using the relative ℓ_2-norm error. Since the solutions are defined on different mesh grids, all electric field data were first interpolated onto a common uniform reference grid defined over the shared computational domain. The relative error was computed by taking the fine mesh solution as the reference, according to

$$e_{\ell_2} = \frac{\|E_{fine}-E_{test}\|_2}{\|E_{fine}\|_2}, \quad (20)$$

where E_{test} denotes the electric field obtained using the normal or the coarse mesh, E_{fine} is the reference electric field obtained from the fine mesh solution and $\|\cdot\|_2$ denotes the ℓ_2-norm. The norm is evaluated over the common reference grid obtained after interpolation over the shared computational domain. The electric field magnitude was selected for the error evaluation, as it directly governs the electrostatic force and particle charging processes.

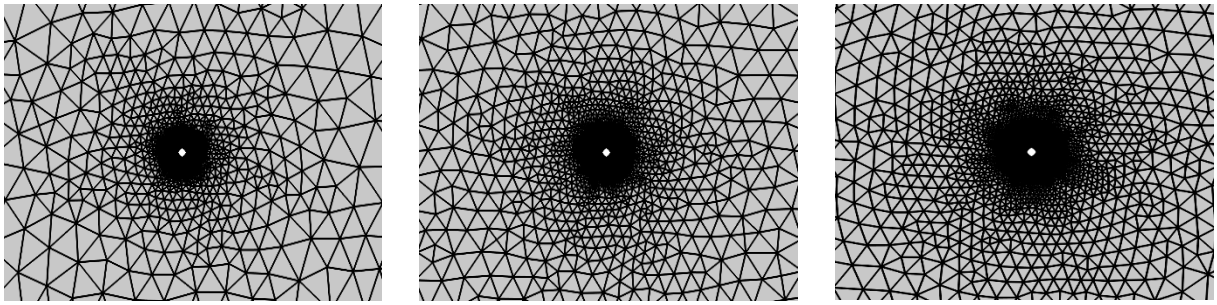

(**a**) (**b**) (**c**)

Figure 2. Unstructured triangular mesh levels used in the mesh independence analysis: (**a**) coarse, (**b**) normal, and (**c**) fine meshes.

The resulting error values for all channel geometries are summarized in Table 2. It is observed that the relative error of the normal mesh remains on the order of 10^{-4} for all cases, whereas the coarse mesh exhibits consistently larger deviations. Nevertheless, even for the coarse mesh, the relative error remains on the order of 10^{-4}, indicating that the solution is already reasonably well resolved. For improved reliability and consistency, the normal mesh was adopted in all subsequent simulations.

Considering the substantially higher computational cost associated with the fine mesh, the normal mesh configuration provides an appropriate balance between numerical accuracy and computational efficiency.

Table 2. Mesh independence results based on the domain-averaged electric field for different channel geometries.

Geometry	ε	Mesh	Nodes	Elements	e_{ℓ_2}
Rectangular channel	0	Coarse	15,095	27,418	8.72×10^{-4}
	0	Normal	19,964	37,142	4.12×10^{-4}
	0	Fine	25,239	47,416	-
Concave channel	0.25	Coarse	15,331	27,474	8.11×10^{-4}
	0.25	Normal	19,827	36,454	4.29×10^{-4}
	0.25	Fine	24,649	45,774	-
Concave channel	0.50	Coarse	13,697	25,114	9.21×10^{-4}
	0.50	Normal	18,713	34,274	5.69×10^{-4}
	0.50	Fine	24,701	45,926	-

Particles were released from the inlet using a regular grid distribution at the start of the transient simulation ($t = 0$). Their trajectories were computed individually using a Lagrangian particle tracking approach [22], ensuring a uniform spatial distribution at the inlet. The initial particle velocity was set equal to the local flow velocity at the inlet:

$$\vec{v}_p(\mathrm{t} = 0) = \vec{u}. \tag{21}$$

Particle–boundary interactions were defined through surface-based criteria. Particles reaching the collecting plates were treated as captured, whereas particles reaching the outlet boundary were treated as escaped. The overall particle collection efficiency was evaluated as

$$\eta = \frac{N_{in} - N_{out}}{N_{in}}. \tag{22}$$

In Equation (22), η is the collection efficiency (%), N_{in} is the total number of injected particles, and N_{out} is the number of particles that reach the outlet [22,26]. It should be noted that particle capture at the collecting plates is assumed to be ideal in the present model. Effects such as particle rebound and re-entrainment are not explicitly considered,

in order to focus on the primary electrohydrodynamic transport and charging mechanisms. While these effects may influence the absolute collection efficiency, they are not expected to alter the qualitative trends associated with geometric modifications.

The electric field distribution inside the electrostatic precipitator was obtained by solving the Poisson equation under appropriate electrical boundary conditions. The boundary conditions were defined according to the classical approach commonly used in electrostatic precipitator modeling [4,5].

The onset of corona discharge at the corona electrode is modeled by specifying the normal component of the electric field at the electrode surface:

$$\vec{n}.\vec{E} = E_0, \tag{23}$$

where $\vec{n}$ is the unit normal vector directed perpendicular to the electrode surface, E_0 is the corona onset electric field. This condition defines the critical electric field required to initiate ionization around the electrode and serves as the criterion for space charge injection into the computational domain [22].

The collecting plates were assumed to be electrically grounded, and the electric potential was set to $V = 0$. A zero normal flux condition was applied for space charge transport at the inlet and outlet boundaries to prevent artificial charge accumulation. To represent the applied high voltage at the corona electrode, the electrode potential was fixed at $V = V_0$. While the fixed potential defines the operating voltage of the electrode, the boundary condition applied to the normal component of the electric field determines the onset of corona discharge and the associated space charge generation. It should be noted that this condition is not imposed as an independent boundary condition for the electric potential; rather serves as a physical onset criterion governing space charge injection. When the local electric field exceeds the onset threshold, charge injection is initiated at the electrode surface.

For the flow field, a constant velocity profile was specified at the inlet and a pressure outlet boundary condition was applied at the outlet. A no-slip wall condition was applied to all solid surfaces. Based on the inlet velocity and the characteristic channel height, the Reynolds number of the flow is approximately $R_e \approx 6.7 \times 10^3$. Although this value lies within the transitional regime, the flow was modeled using a laminar formulation due to the relatively low inlet velocity and the smooth channel geometry considered in the present configuration.

To evaluate the influence of turbulence modeling, additional simulations were performed using the $k-\omega$ SST turbulence model for the concave channel geometry ($\varepsilon = 0.25$). The velocity fields obtained from the laminar and turbulent solutions are compared in Figure 3. The predicted velocity magnitude distribution exhibited only minor differences compared with the laminar solution, while the overall flow structure remained essentially unchanged. These observations indicate that the laminar formulation provides an adequate representation of the flow behavior for the present ESP configuration.

The corona onset electric field E_0 was calculated using Peek's empirical corona onset relation, which is widely used in the literature to represent realistic physical conditions:

$$E_0 = 3 \times 10^6 \delta \left(1 + \frac{0.03}{\sqrt{\delta r_i}}\right), \tag{24}$$

where δ is the gas density correction factor, and r_i is the radius of the corona electrode [5,22].

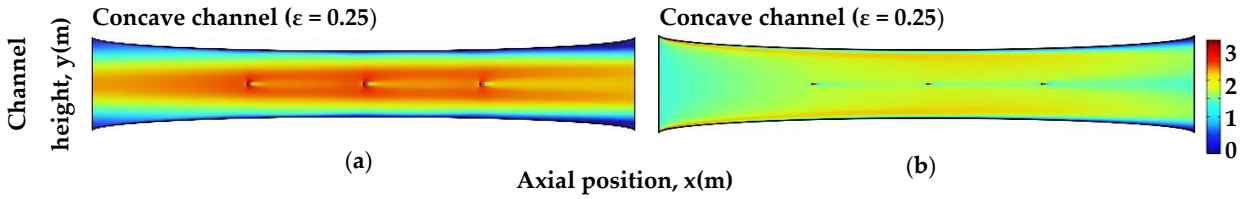

Figure 3. Comparison of velocity magnitude distributions for the concave channel geometry (ε = 0.25): (a) laminar flow solution and (b) $\boldsymbol{k-\omega}$ SST turbulence model.

Particle transport within the electrostatic precipitator is a multi-physics process resulting from the simultaneous interaction of the electric field, space charge transport, gas flow, and particle dynamics. Therefore, the modeling was performed within a coupled numerical framework based on classical electromagnetic field theory and electrohydrodynamic flow principles [8,29]. All physical fields were solved simultaneously within the same solution environment.

The flow field, electrostatic field, and space-charge transport were described by the Navier–Stokes, Poisson, and continuity equations, respectively, and solved in a coupled framework to capture the interaction among the physical fields. All simulations were performed using COMSOL Multiphysics. The electrostatic potential was obtained by solving the Poisson equation with prescribed electrode potentials. The onset of corona discharge at the electrode surface was described using Peek's empirical relation for the corona onset electric field, which determines the ion injection at the electrode surface and provides the source of space charge within the domain. The resulting space-charge distribution was then coupled to the electrostatic field through the Poisson equation, and the governing equations for the electric field and charge transport were solved iteratively until convergence was achieved. This coupled solution framework enables consistent representation of the interactions among the electric field, space-charge transport, and electrohydrodynamic flow within the ESP channel.

The finite element method (FEM) was employed because of its capability to accurately represent complex geometries and various boundary conditions. Specifically, the governing equations were discretized using FEM and solved using a stationary nonlinear solver based on Newton's method within the COMSOL Multiphysics environment. The FEM provides a robust numerical approach for solving nonlinear and multi-physics problems [30,31]. During the solution process, a fully coupled nonlinear solver was adopted to enhance numerical stability and facilitate convergence of the governing equations.

3. Results and Discussion

This section presents the numerical results and discusses the influence of channel geometry on the coupled electrohydrodynamic processes inside the electrostatic precipitator. First, the reliability of the numerical model is assessed through comparison with literature data. Subsequently, the flow field characteristics are analyzed to examine how the concave geometry modifies the velocity distribution within the channel. The pressure drop behavior is then evaluated to assess the hydraulic implications of the proposed geometry. The electric field structure and space charge distribution are further investigated to clarify the underlying electrostatic mechanisms. Finally, particle charging behavior, particle trajectories, and overall collection efficiency are analyzed to evaluate the impact of the concave channel design on ESP performance. For comparison, an additional Venturi-like contraction geometry is also examined to highlight the differences in ion transport, charging region development, and overall particle collection behavior.

3.1. Model Validation

To assess the reliability of the numerical model, the simulation results were qualitatively compared with previously published studies. As shown in Figure 4, the model successfully captures the variation in collection efficiency with inlet flow velocity reported in the literature [26].

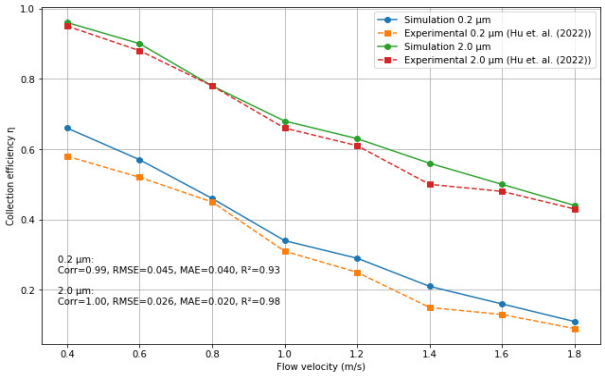

Figure 4. Comparison of collection efficiency as a function of inlet flow velocity between the present simulation results and literature data [26].

Specifically, the collection efficiency decreases with increasing flow velocity as particle residence time in the electrostatic field is reduced. This trend is consistent for both 0.2 μm and 2.0 μm particles and agrees well with the literature. Minor differences arise from modeling assumptions, boundary conditions, and the two-dimensional approximation. Overall, the results demonstrate that the proposed model reliably predicts particle collection behavior in electrostatic precipitators.

3.2. Flow Field Analysis

To evaluate the flow behavior inside the electrostatic precipitator channel, the velocity magnitude distributions obtained for different channel geometries were examined. Figure 5 illustrates how the velocity field is redistributed depending on the channel geometry under different applied voltage levels.

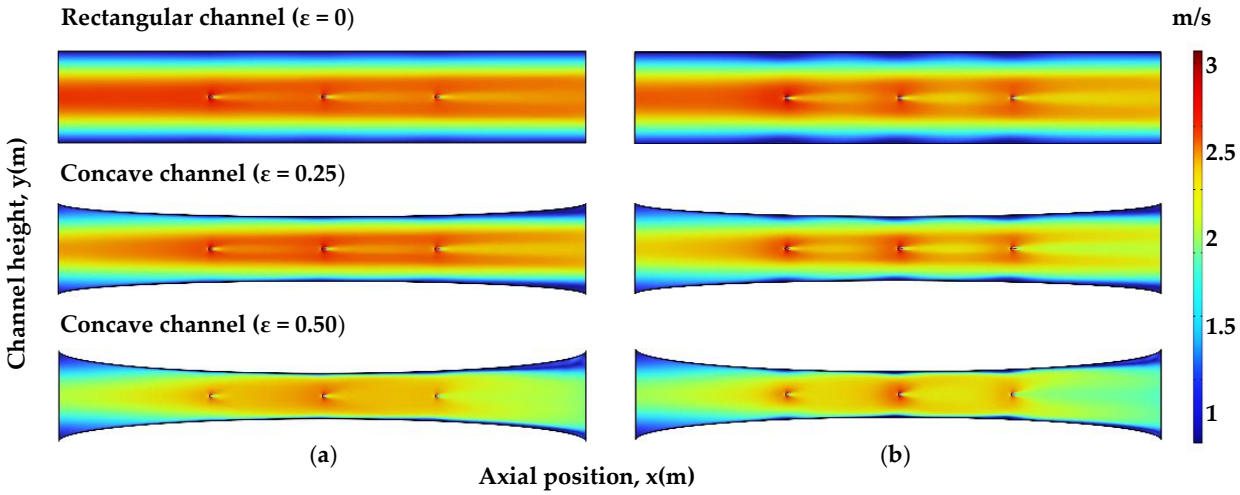

Figure 5. Velocity magnitude distributions for different channel geometries in the electrostatic precipitator channel: (**a**) 20 kV and (**b**) 25 kV.

Channel geometry directly controls the internal flow structure within the filter by reshaping the velocity distribution through local contractions and expansions along the

flow cross-section. As shown in Figure 3, the flow in the rectangular channel configuration exhibits a relatively uniform structure along the channel, whereas in concave geometries, distinct acceleration regions appear in the central zone due to the local contraction of the cross-section. The local contraction of channel cross-section leads to flow acceleration due to mass conservation, resulting in higher velocity gradients near the channel center. Under steady incompressible flow conditions, mass conservation requires that the product of the cross-sectional area and the mean velocity remain approximately constant along the channel. Therefore, the local contraction of the channel geometry leads to an increase in the flow velocity in the narrowed region. This acceleration produces stronger velocity gradients within the contraction region and alters the flow structure inside the channel. Such changes in the velocity field can influence the aerodynamic drag acting on particles and, consequently, affect particle transport and migration toward the collecting surfaces. The limited increase in the voltage on velocity field indicates that electrohydrodynamic (EHD) forces remain relatively weak compared to inertia of the main gas flow under the present operating conditions.

3.3. Pressure Drop Characteristics

The influence of channel geometry on flow resistance was evaluated using the average static pressure difference between the inlet and outlet sections. The pressure drop was defined as $\Delta p = p_{inlet} - p_{outlet}$ based on the line-averaged static pressure values. Under the 20 kV operating condition, the pressure drop was calculated as 1.94×10^{-1} Pa for the rectangular channel, 3.71×10^{-1} Pa for the concave channel with $\varepsilon = 0.25$, and 6.75×10^{-1} Pa for the concave channel with $\varepsilon = 0.50$. These values are relatively small compared with those reported for full-scale ESP systems, primarily due to the limited channel length and the simplified two-dimensional geometry adopted in the present numerical model. A similar trend was observed at the 25 kV voltage level, where the pressure drop increased moderately with increasing channel concavity. The results indicate that modifications of the channel geometry influence electrostatic performance without introducing a substantial increase in hydrodynamic energy consumption. Although the concave geometry introduces local contractions in the flow passage, the overall pressure drop remains limited because the contraction occurs only over a restricted portion of the channel and does not significantly reduce the average cross-sectional area. This characteristic is desirable in electrostatic precipitator design, where maintaining low pressure losses is essential for minimizing fan power consumption. The results, therefore, suggest that concave channel geometries can improve particle collection efficiency while preserving the inherently low energy consumption of ESP systems.

3.4. Electric Field Distribution

The electric field distribution is a key factor governing particle motion inside an electrostatic precipitator. To evaluate the influence of channel geometry on the electric field structure, the electric field magnitude distributions for different channel configurations were compared while keeping the electrode configuration identical in all cases. The electric field distributions calculated at operating voltages of 20 kV and 25 kV are presented in Figure 6.

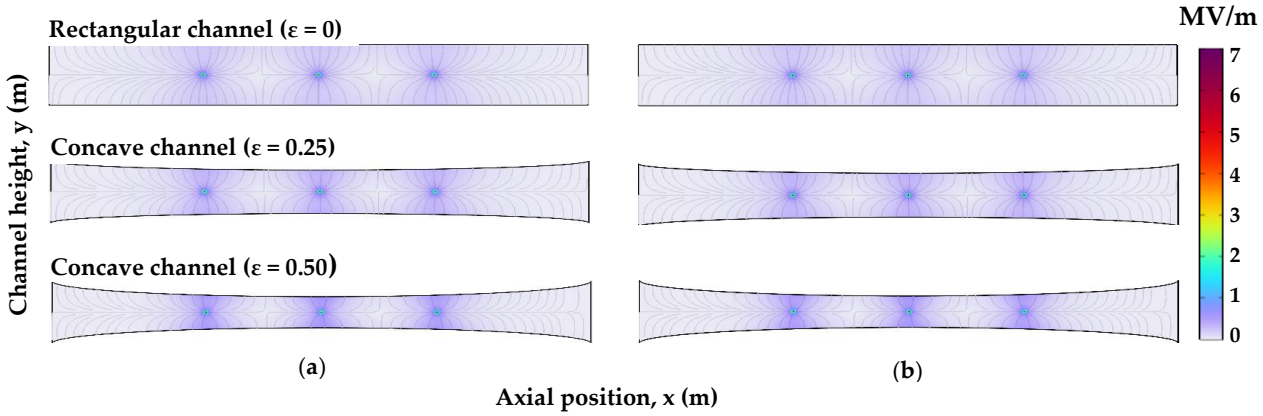

Figure 6. Electric field magnitude distributions for different channel geometries in the electrostatic precipitator channel under operating voltages of (**a**) 20 kV and (**b**) 25 kV.

As expected, the highest electric field intensity occurs in the vicinity of the corona electrodes, which is consistent with the classical behavior of wire–plate electrostatic precipitators. The peak field magnitude remains nearly unchanged for all channel geometries because it is primarily determined by the electrode configuration rather than the channel shape. However, the spatial distribution of the field within the channel is noticeably influenced by the concave geometry. The local contraction of the channel modifies the electrode–plate distance and alters the arrangement of the equipotential lines, leading to a redistribution of the electric field within the channel volume. To quantify the spatial variation in the electric field distribution, the coefficient of variation (CV) was used as a measure of field uniformity [32]. The CV is defined as

$$\mathrm{CV} = \frac{\sigma_E}{E_{avg}}, \tag{25}$$

where σ_E denotes the standard deviation of the electric field magnitude and E_{avg} represents the average electric field over the computational domain. Lower CV values indicate a more uniform electric field distribution.

The quantitative results presented in Table 3 show that, although the maximum electric field magnitude remains almost constant, the average electric field intensity increases in the concave channel configurations. This behavior indicates that the electric field extends more effectively into the channel core in comparison with the rectangular configuration. The coefficient of variation values further confirm that the electric field remains strongly nonuniform due to the localized high-intensity region near the corona electrodes. Nevertheless, the concave geometry improves the effective utilization of the electric field by increasing its average magnitude within the channel volume. This redistribution of the electric field plays an important role in particle transport because an increase in the average electric field intensity enhances particle charging and strengthens the electrostatic force acting on the particles. In addition, the stronger electric field within the channel core promotes deeper ion transport and a broader space-charge distribution, which further enhances the ion–particle interaction within the flow domain. Consequently, the modified field structure promotes particle migration toward the collecting plates and contributes to the improved collection efficiency observed in the concave channel configurations.

Table 3. Statistical comparison of the electric field magnitude for different channel geometries.

Geometry	Voltage (kV)	Max. Electric Field (V/m)	Average Electric Field (V/m)	Standard Deviation σ_E(V/m)	CV (σ_E/E_{avg})
Rectangular channel ($\boldsymbol{\varepsilon = 0}$)	20	7.03×10^6	9.87×10^4	1.18×10^5	1.19
Rectangular channel ($\boldsymbol{\varepsilon = 0}$)	25	7.03×10^6	1.55×10^5	1.44×10^5	0.93
Concave channel ($\boldsymbol{\varepsilon = 0.25}$)	20	7.03×10^6	1.15×10^5	1.49×10^5	1.30
Concave channel ($\boldsymbol{\varepsilon = 0.25}$)	25	7.03×10^6	1.73×10^5	1.94×10^5	1.12
Concave channel ($\boldsymbol{\varepsilon = 0.50}$)	20	7.03×10^6	1.24×10^5	1.85×10^5	1.49
Concave channel ($\boldsymbol{\varepsilon = 0.50}$)	25	7.03×10^6	1.81×10^5	2.42×10^5	1.34

3.5. Space Charge Density Distribution

The space charge density distribution reveals the transport behavior of ions generated by corona discharge inside the channel. To examine the influence of channel geometry on ion transport, space charge density distributions obtained at operating voltages of 20 kV and 25 kV are compared for rectangular ($\varepsilon = 0$), 25% concave ($\varepsilon = 0.25$), and 50% concave ($\varepsilon = 0.50$) channel geometries, as shown in Figure 7.

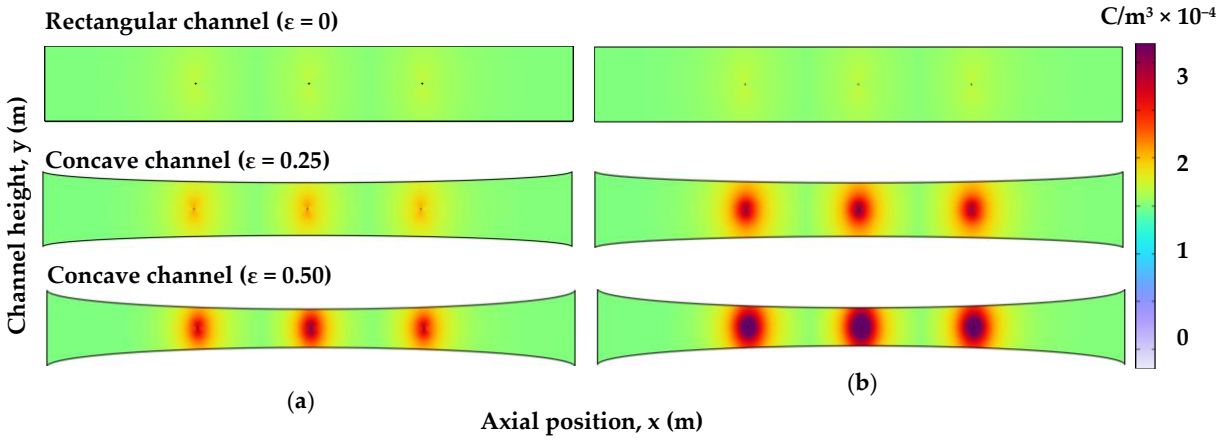

Figure 7. Space charge density distributions for rectangular and concave channel geometries in the electrostatic precipitator under operating voltages of (**a**) 20 kV and (**b**) 25 kV.

As shown in Figure 7, the space charge density in the rectangular channel geometry is primarily concentrated around the corona electrodes and rapidly decreases throughout the channel volume. This behavior indicates limited ion penetration, resulting in an electrostatic interaction region confined to localized areas. When concavity is introduced into the channel geometry, the space charge distribution expands across the flow cross-section. For $\varepsilon = 0.25$ and $\varepsilon = 0.50$, the enhanced ion transport leads to an increase in the electrohydrodynamic interaction volume within the channel. The enhanced space charge dispersion observed in concave channel geometries can also be associated with the modification of the internal flow field. As shown in the flow analysis, the local contraction of the channel accelerates the gas velocity due to mass conservation. This increased velocity enhances the convective transport of ions represented by the $\rho_q \vec{u}$ term in the charge transport equation (see Equation (11)). Consequently, ions penetrate further into the channel volume, expanding the electrohydrodynamic interaction region. This extended ion

distribution promotes earlier particle charging and contributes to the improved particle migration and collection efficiency observed for concave geometries. Increasing the applied voltage from 20 kV to 25 kV leads to an increase in the magnitude of the space charge density, while the overall distribution pattern remains largely unchanged.

This behavior suggests that the channel geometry, rather than the applied voltage, primarily governs the topology of the space-charge field. A quantitative comparison of the obtained distributions is presented in Table 4. To further evaluate the degree of space charge dispersion within the channel volume, the uniformity index (UI) was employed, defined as UI = ρ_{avg}/ρ_{max} [32]. The results indicate that channel geometry plays a decisive role in determining the spatial distribution of space charge and the associated ion transport within the channel. These findings suggest that geometric modifications influence not only the flow and electric field structures but also regulate ion transport, thereby directly affecting the electrohydrodynamic interaction volume.

Table 4. Statistical comparison of space charge density and uniformity index for different channel geometries at operating voltages of 20 kV and 25 kV.

Voltage (kV)	Geometry	ρ_{avg} (C/m³)	ρ_{max}(C/m³)	Uniformity Index (UI = ρ_{avg}/ρ_{max})
20	$\varepsilon = 0.00$	1.1239×10^{-5}	3.9340×10^{-5}	0.286
20	$\varepsilon = 0.25$	2.2049×10^{-5}	1.2479×10^{-4}	0.177
20	$\varepsilon = 0.50$	3.5625×10^{-5}	3.4035×10^{-4}	0.105
25	$\varepsilon = 0.00$	2.6641×10^{-5}	1.3531×10^{-4}	0.197
25	$\varepsilon = 0.25$	4.3171×10^{-5}	3.4434×10^{-4}	0.125
25	$\varepsilon = 0.50$	6.2738×10^{-5}	8.1616×10^{-4}	0.077

Table 4 further shows a substantial increase in the maximum space-charge density with increasing channel concavity, indicating enhanced ion accumulation within the channel. As indicated by the electrohydrodynamic body-force term in Equation (6), an increase in space-charge density strengthens the coupling between the electric and flow fields. Increased ion concentration also accelerates particle charging, which promotes particle migration toward the collecting plates and leads to improved collection efficiency in concave channel configurations. Although elevated space-charge levels may potentially cause electric-field shielding in ESP systems, such shielding requires localized charge accumulation near the discharge electrode; in the present results, however, enhanced ion transport redistributes the space charge, leading to an expansion of the electrostatic interaction region rather than its suppression.

3.6. Particle Trajectories and Charging Behavior

Particle tracking analysis was performed to evaluate the influence of channel geometry on particle transport and collection behavior. Particle motion inside the ESP channel is governed by the combined effects of aerodynamic drag and electrostatic forces acting on charged particles. As particles travel along the channel, they progressively accumulate electric charge through ion–particle interactions, which increases the electrostatic force acting on them. Consequently, particle trajectories gradually deviate toward the collecting plates under the influence of the electric field. The trajectories corresponding to different particle sizes are presented in Figures 8–11.

As shown in Figures 8–11, particles initially enter the channel with relatively low charge levels and therefore follow the streamlines of the carrier flow in the upstream region. As the particles move downstream, continuous ion–particle interactions lead to an increase in the accumulated particle charge, which strengthens the electrostatic migration

toward the collecting surfaces. As a result, the deviation of the particle trajectories becomes more pronounced along the axial direction as the charging process progresses.

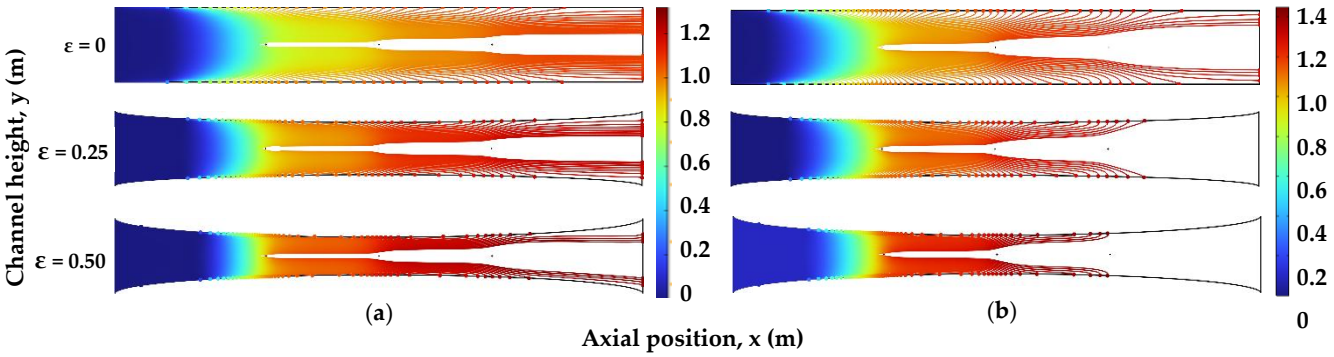

Figure 8. Particle trajectories for $\boldsymbol{\varepsilon = 0, 0.25, 0.50}$ at $\boldsymbol{r_p = 0.01}$ μm: (**a**) **20** kV, (**b**) **25** kV.

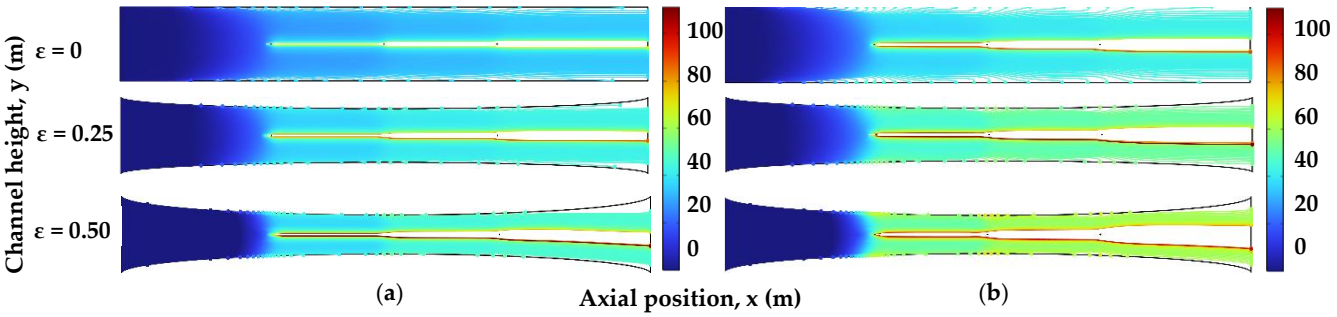

Figure 9. Particle trajectories for $\boldsymbol{\varepsilon = 0, 0.25, 0.50}$ at $\boldsymbol{r_p = 0.02}$ μm: (**a**) **20** kV, (**b**) **25** kV.

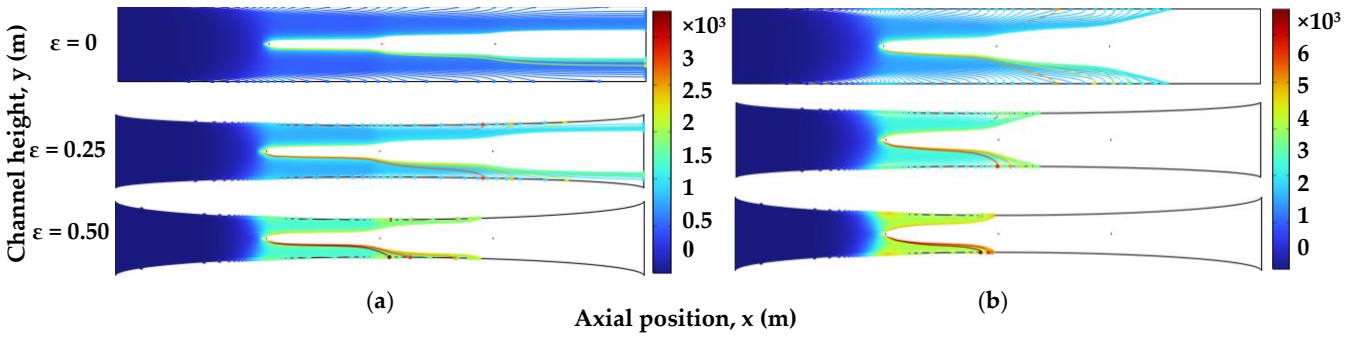

Figure 10. Particle trajectories for $\boldsymbol{\varepsilon = 0, 0.25, 0.50}$ at $\boldsymbol{r_p = 2}$ μm: (**a**) **20** kV, (**b**) **25** kV.

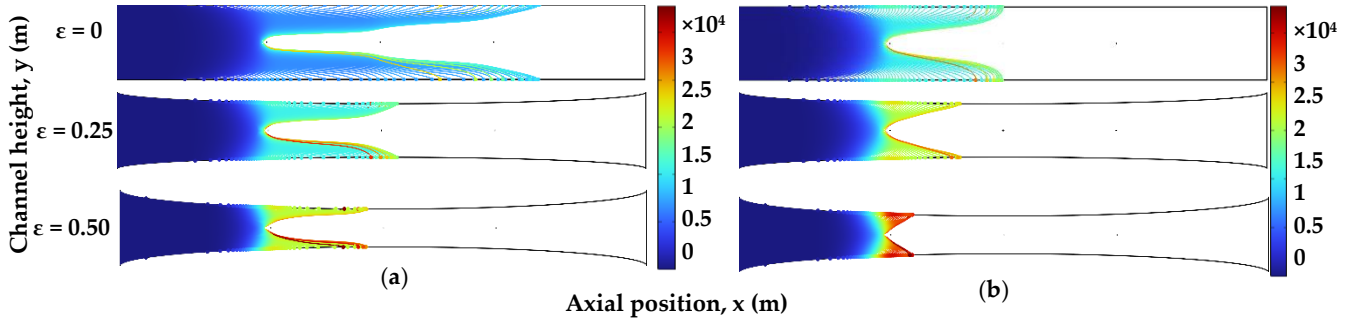

Figure 11. Particle trajectories for $\boldsymbol{\varepsilon = 0, 0.25, 0.50}$ at $\boldsymbol{r_p = 5}$ μm: (**a**) **20** kV, (**b**) **25** kV.

The applied voltage has a direct influence on the particle charging rate. Increasing the operating voltage enhances the electric field intensity and ion concentration within the channel, which accelerates particle charging and increases the electrostatic force acting on

the particles. Consequently, particles deviate toward the collecting plates earlier along the channel length under higher voltage conditions.

Channel geometry also plays an important role in determining particle transport behavior. In concave channel configurations, the modified flow structure and enhanced ion penetration into the channel core led to stronger ion–particle interactions compared with the rectangular channel configuration. This enhanced ion transport promotes faster particle charging and results in stronger trajectory deviation toward the collecting surfaces. The earlier trajectory deviation observed in concave geometries is consistent with the increased ion penetration and space charge levels discussed in Section 3.4.

Particle size further affects the balance between aerodynamic drag and electrostatic force. Smaller particles accumulate lower charge levels and therefore tend to follow the flow streamlines for a longer distance before deviating toward the collecting plates. In contrast, larger particles acquire higher charge levels and experience stronger electrostatic forces, which leads to earlier deviation and faster migration toward the collecting surfaces. The stronger trajectory deviation observed for larger particles is consistent with the field charging mechanism typically dominant in electrostatic precipitators, where particle charge increases with particle size under strong electric fields.

The trajectory patterns shown in Figures 7–10 also indicate that particle deviation toward the collecting plates occurs earlier along the channel in concave geometries. This behavior can be interpreted in terms of the electrostatic migration length of particles. As particles accumulate charge through ion–particle interactions, the electrostatic migration velocity increases and the characteristic migration length required for particles to reach the collecting plates decreases. The enhanced ion penetration and higher space charge levels observed in concave channel configurations therefore reduce the migration length, causing particles to deviate toward the collecting plates earlier compared with the rectangular channel configuration.

3.7. Accumulated Charge Number

To quantitatively evaluate the transport behavior observed in the particle trajectory analysis, the accumulated charge number acquired by particles along the channel was analyzed. The accumulated charge number was calculated at the final simulation time step and compared for different channel geometries and operating voltages as a function of particle radius. The resulting accumulated charge distributions are presented in Figure 12.

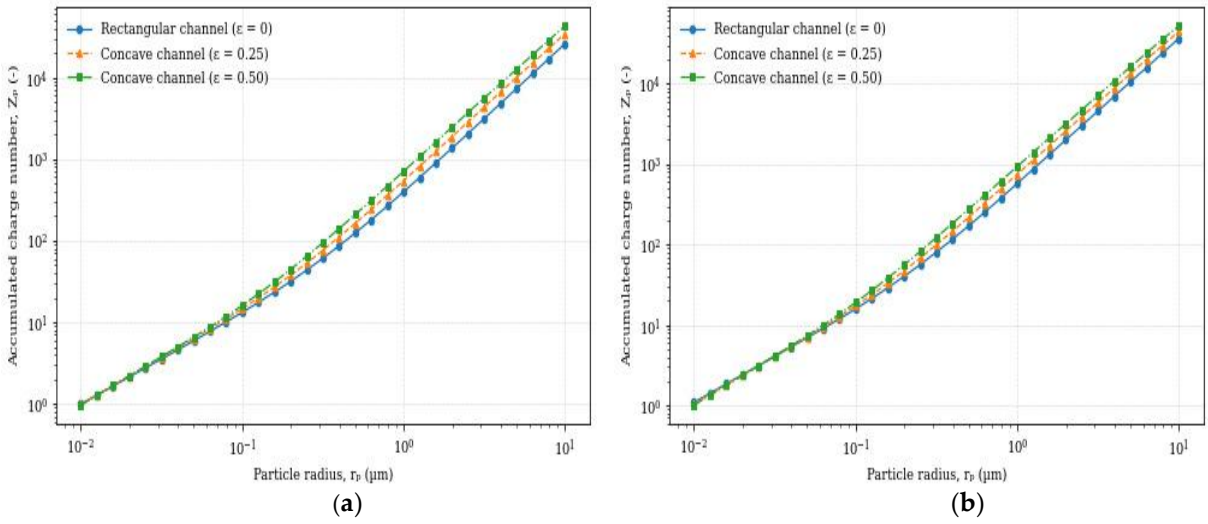

Figure 12. Average accumulated charge number as a function of particle radius for different channel geometries: (**a**) 20 kV, (**b**) 25 kV.

The parameter Z denotes the dimensionless accumulated charge number defined as the ratio of the particle charge (q_p) to the elementary charge e, i.e., $Z = q_p/e$.

The increase in the accumulated charge number observed for concave channel geometries is consistent with the expanded space charge distribution presented in Figure 7. As ions are transported further into the channel volume due to enhanced convective transport, particles experience higher ion exposure along their trajectories. This increased ion–particle interaction leads to higher accumulated particle charge levels, which strengthens the electrostatic force acting on the particles and promotes their migration toward the collecting plates. This trend is further quantified in Table 5.

To further clarify the mechanism underlying the improved collection of 0.1 μm particles, Table 5 provides a quantitative comparison of particle dynamics for the rectangular and concave channel geometries. Although the residence time decreases from the rectangular to the concave channel geometries, both the accumulated charge number and the charging rate increase significantly with the contraction ratio. This behavior indicates that the enhanced ion transport in the concave channels accelerates particle charging despite the shorter residence time. Consequently, the EHD force acting on the particles increases substantially, promoting stronger migration toward the collecting plates and improving collection efficiency. These results demonstrate that the improvement in submicron particle collection is governed primarily by enhanced charging kinetics and stronger EHD interaction, rather than by residence time alone.

Table 5. Quantitative comparison of EHD-driven particle dynamics for 0.1 μm particles under different channel geometries.

Geometry	Residence Time (s)	Charge Number Z (-)	Charging Rate (Z/s)	EHD Force (N/m³)	Particle Force (N)	Efficiency (%)
Rectangular	0.75	13.25	17.67	1.87	1.11×10^{-13}	32
Concave (ε = 0.25)	0.51	14.95	29.31	5.48	2.29×10^{-13}	42
Concave (ε = 0.50)	0.41	16.85	41.10	12.80	4.38×10^{-13}	52

3.8. Fractional Collection Efficiency

To evaluate the effect of variations observed in particle loading on electrostatic precipitator performance, the collection efficiency as a function of particle radius was examined for different channel geometries. In this context, collection efficiency is analyzed in a fractional (size-resolved) manner.

The collection efficiency results obtained under operating voltages of 20 kV and 25 kV are presented in Figure 13.

The collection efficiency curves exhibit the characteristic U-shaped behavior commonly observed in electrostatic precipitators. A minimum efficiency region occurs for intermediate particle sizes around $r_p \approx 0.1$ μm, where both electrostatic charging and diffusion mechanisms become relatively ineffective. For smaller particles, Brownian diffusion enhances particle deposition onto the collecting plates, whereas for larger particles the increasing electrostatic force significantly promotes particle migration toward the collecting surfaces.

The concave channel geometries consistently show higher collection efficiency across the entire particle size range compared with the rectangular channel. This improvement becomes particularly significant in the minimum-efficiency region, where the concave geometry increases the efficiency by more than 20 percentage points. The enhanced performance is attributed to improved ion penetration and stronger particle charging resulting from the modified flow and electric field distribution inside the channel. These results suggest that ESP channel geometries that promote ion penetration into the channel core

can significantly enhance particle charging and mitigate the minimum-efficiency region characteristic of conventional ESP configurations.

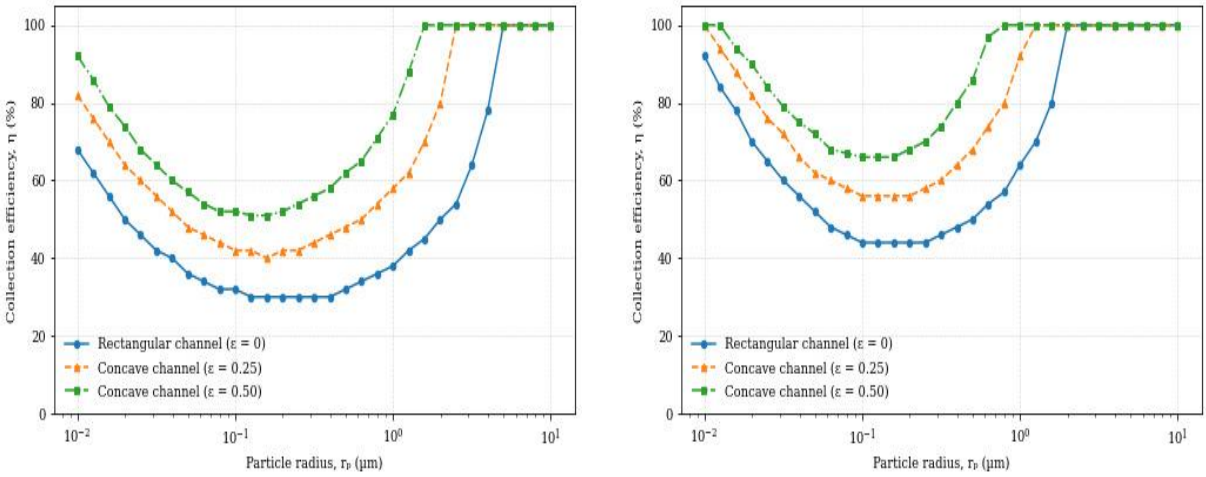

Figure 13. Fractional collection efficiency as a function of particle radius for different channel geometries at applied voltages of (**a**) 20 kV and (**b**) 25 kV.

3.9. Quantitative Assessment of Convective and Drift Transport Contributions

To provide a quantitative assessment of the relative importance of convective and drift transport, an additional indicator was introduced based on the local ratio between flow velocity and ion drift velocity, defined as

$$R = \frac{|\vec{u}|}{\mu_i |\vec{E}|}, \tag{26}$$

where $|\vec{u}|$ denotes the local gas velocity magnitude, μ_i is the ion mobility, and $|\vec{E}|$ is the electric field magnitude. This parameter provides a relative measure of the local contribution of convection compared to ion drift. Figure 14 presents the spatial distribution of R for different channel geometries.

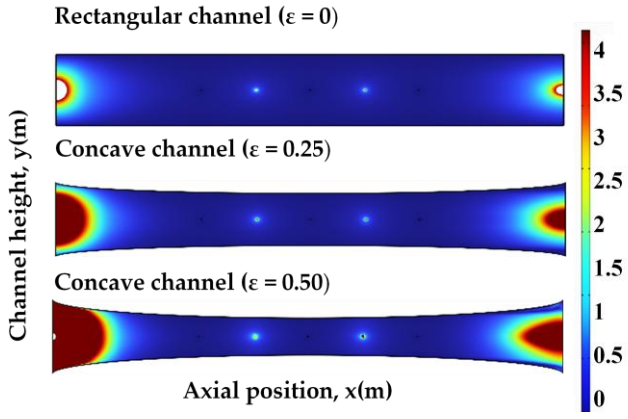

Geometry	u/(μ$_i$E) (–)
Rectangular (ε = 0)	0.29
Concave (ε = 0.25)	0.82
Concave (ε = 0.50)	3.37

Figure 14. Spatial distribution of the convection-to-drift transport ratio ($|\vec{u}|/(\mu_i|\vec{E}|)$) for different channel geometries, together with the corresponding averaged values.

The results show that ion transport in the rectangular configuration remains predominantly drift-driven, as indicated by relatively low R values. In contrast, the concave channel geometries exhibit substantially higher values of this parameter, particularly in the channel core, indicating an increased relative contribution of convective transport.

To further quantify this behavior, the average R values are presented here. The results indicate that this parameter increases from 0.29 for the rectangular channel to 0.82 and 3.37 for the concave geometries as the with contraction ratio increases. This systematic increase demonstrates that geometry-induced flow modification enhances the relative contribution of convective transport compared to ion drift.

These findings provide a quantitative visualization of the convection-to-drift balance and further support the observed geometry-dependent electrohydrodynamic behavior.

3.10. Comparison with a Venturi-like Contraction

To further understand the influence of channel geometry on the electrohydrodynamic behavior inside the electrostatic precipitator, an additional comparative analysis was performed using a Venturi-like channel configuration as illustrated in Figure 14. Unlike the smooth concave geometry examined in the previous sections, the Venturi-like geometry introduces a piecewise contraction and expansion along the flow direction, resulting in an abrupt reduction in the channel cross-section followed by a rapid expansion. This configuration allows the influence of smooth geometric variation to be distinguished from that of a simple cross-sectional contraction.

Figure 15 presents the velocity magnitude distribution obtained for the Venturi-like geometry. Due to the abrupt reduction in the channel cross-section, the flow undergoes strong local acceleration in the throat region, producing a high-velocity flow region near the channel centerline. This behavior is consistent with the mass conservation principle for incompressible flow, where a reduction in cross-sectional area leads to an increase in local velocity. Compared with the concave channel geometry, the acceleration in the Venturi-like configuration is more localized and produces stronger velocity gradients near the contraction region.

The corresponding electric field magnitude distribution is shown in Figure 16. In this configuration, the contraction modifies the local electrode–plate spacing and leads to a concentration of the electric field near the throat region. As a result, the electric field becomes more localized around the contraction zone rather than being distributed more broadly across the channel volume.

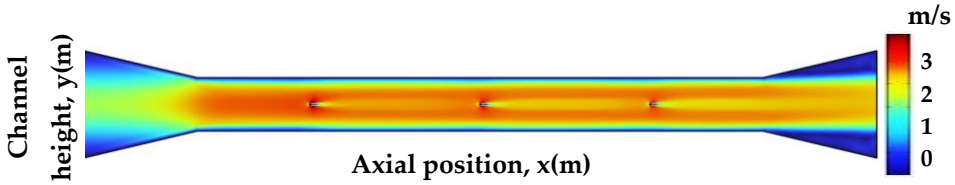

Figure 15. Velocity magnitude distribution along the Venturi-like channel.

Figure 16 illustrates the resulting space charge density distribution. In the Venturi-like geometry, the ion cloud remains concentrated primarily in the vicinity of the electrodes and the throat region, indicating limited ion penetration into the central flow region. In contrast, the smooth concave channel geometry promotes a broader spatial distribution of ions within the channel, allowing the electrostatic interaction region to extend further into the core flow. The resulting space charge density distribution is presented in Figure 17.

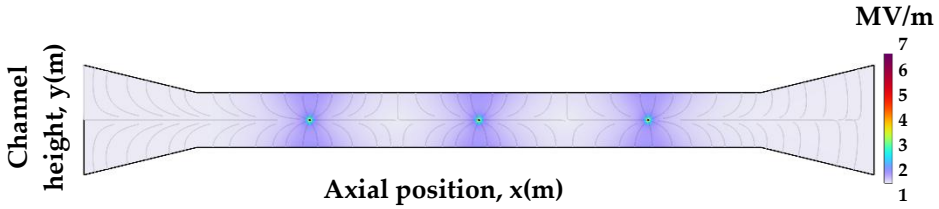

Figure 16. Electric field magnitude distribution along the Venturi-like channel.

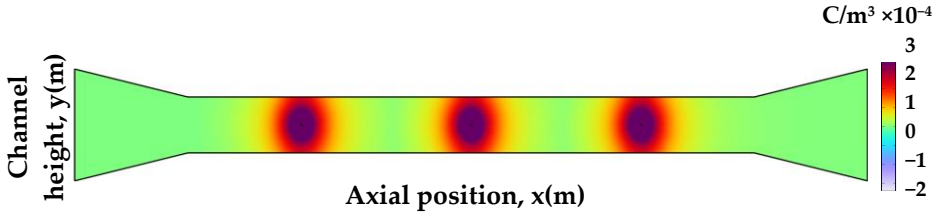

Figure 17. Space charge density distribution along the Venturi-like channel.

These observations suggest that the performance improvement observed in the concave channel geometry is not simply caused by the reduction in the channel cross-section. Instead, the key mechanism appears to be the smooth redistribution of the electric field and ion transport within the channel volume, which increases the effective interaction region between ions and particles. The Venturi-like configuration, despite introducing a stronger local contraction, does not provide the same spatial expansion of the electrohydrodynamic interaction region. Consequently, the results indicate that smooth geometric variation can enhance field utilization and ion penetration without producing excessive flow acceleration or localized electric field concentration, thereby offering a more effective strategy for improving electrostatic precipitator performance.

3.11. Overall Performance Evaluation

The combined analyses of the flow field, electric field distribution, space charge transport, and particle trajectories provide a consistent physical explanation for the improved performance observed in concave channel geometries. The concave configuration introduces a gradual geometric contraction that modifies the internal flow structure and enhances the convective transport of ions generated at the corona electrodes. Consequently, ions penetrate more effectively into the channel core, resulting in higher space charge levels and stronger ion–particle interactions within the flow domain.

The increased ion availability promotes faster particle charging along the channel. Particles, therefore, experience stronger electrostatic forces and migrate more rapidly toward the collecting plates. Particle trajectory analysis shows that the enhanced charging leads to earlier deviation of particle paths toward the plates and reduces the effective migration distance required for particle capture. These effects result in higher collection efficiency compared with the conventional rectangular channel configuration.

The improved electrostatic performance is achieved without a significant increase in pressure drop. The concave channel geometry enhances particle collection while preserving the inherently low energy consumption characteristic of electrostatic precipitators. Geometric modification of ESP channels thus provides an effective passive design strategy for improving particulate removal performance.

For comparison, a Venturi-like channel geometry was also examined. In this configuration, the local contraction increases the flow velocity and consequently enhances the convective transport of ions generated at the corona electrodes. At first glance, this increased convection may appear beneficial for ion transport within the channel. However,

the strong, abrupt acceleration in the throat region rapidly carries the ions through a narrow zone, resulting in a highly concentrated space charge distribution. Therefore, the ion–particle interaction volume remains limited. The high convection velocity also reduces the effective residence time of particles within the ion-rich region, thereby limiting particle charging. Consequently, despite locally enhanced ion convection, the overall charging process becomes less effective, leading to reduced particle migration and lower ESP collection efficiency.

In contrast, the smooth concave geometry introduces a gradual variation in the channel cross-section, producing a smoother redistribution of both the velocity and electric fields. The gradual acceleration enhances ion convection without generating strong localized high-velocity regions. As a result, ions penetrate more effectively into the channel core, producing a broader spatial distribution of space charge. The enlarged ion–particle interaction region increases the probability of particle charging and promotes stronger electrostatic migration toward the collecting plates. Accordingly, the increase in ion convection becomes advantageous in the concave configuration because it occurs together with an expanded charging region within the channel.

4. Conclusions

This study demonstrates that the proposed elliptical smooth-gradient concave geometry offers a distinct approach to improving ESP performance by controlled modification of the flow–field interaction. The use of contraction ratio as a governing parameter enables quantitative regulation of electrohydrodynamic (EHD) coupling, leading to enhanced particle charging and transport behavior. In addition, the simplicity of the geometry represents an engineering advantage, offering practical implementation in existing ESP systems with low retrofit complexity.

The results demonstrate that channel geometry plays a critical role in governing EHD coupling and particle collection. While the peak electric field magnitude remains primarily determined by the electrode configuration, geometric modifications alter the spatial distribution of the electric field and the transport of space charge within the channel. Specifically, the concave configuration enhances ion penetration into the channel core and expands the ion–particle interaction region, leading to faster particle charging and earlier particle migration toward the collecting plates. Accordingly, the proposed elliptical smooth-gradient concave channel significantly improves submicron particle collection, increasing the efficiency for 0.1 μm particles from approximately 30% in the rectangular configuration to about 50% at higher contraction ratios ($\varepsilon = 0.50$), corresponding to an improvement of nearly 20 percentage points.

Active control strategies, such as pulsed power supply and electrode optimization, can enhance ESP performance by modifying electrical and flow conditions [33,34], but often at the expense of increased system complexity and operational cost. In contrast, passive design parameters, such as channel geometry, offer a complementary and cost-effective approach by influencing electrohydrodynamic interactions without additional energy input. The proposed concave channel configuration thus provides a simple and easily implementable solution for improving ESP performance.

A comparison with a Venturi-like contraction highlights the importance of geometric smoothness. While the Venturi geometry induces strong local acceleration, the resulting localized space-charge distribution and reduced particle residence time limit effective particle charging. In contrast, the smooth concave geometry promotes a more distributed electrohydrodynamic (EHD) interaction region, leading to improved particle charging and collection. The results further indicate that the contraction ratio serves as a practical quantitative parameter for regulating flow–field interaction, while the simplicity of the proposed geometry enables low-cost integration into existing ESP systems.

https://doi.org/10.3390/app16094356

Overall, the findings indicate that channel geometry constitutes an important passive design parameter for electrostatic precipitators. The concave configuration enhances particle collection performance while maintaining the inherently low pressure drop characteristic of ESP systems.

In addition, incorporating realistic particle properties and particle–surface interaction models, along with experimental validation, would further strengthen the findings. Integration with data-driven approaches, such as machine learning [35], may also enable efficient multi-parameter optimization and reduced computational cost.

While three-dimensional effects, such as end effects and spanwise vortical structures, may locally influence the flow field and particle trajectories, the main conclusions of this study are governed primarily by cross-sectional electrohydrodynamic interactions. Future work may extend the present framework to fully three-dimensional configurations to capture such effects more accurately. While alternative smooth geometries, such as sinusoidal or polynomial profiles, may lead to different electrohydrodynamic behavior, a systematic comparison of different smooth curve families is beyond the scope of the present study and is identified as an important direction for future research.

Author Contributions: Conceptualization, H.K., G.K.E., I.T. and A.S.; methodology, H.K., G.K.E. and I.T.; software, H.K.; formal analysis, H.K., O.A.S. and A.S.; investigation, H.K.; resources, I.T. and G.G.; data curation, H.K. and G.K.E.; writing—original draft preparation, H.K.; writing—review and editing, A.S., G.G. and O.A.S.; visualization, H.K.; supervision, I.T., G.K.E. and G.G. All authors have read and agreed to the published version of the manuscript.

Funding: This study was supported by the Scientific Research Projects Committee of Marmara University (BAPKO) under Grant No. FDK-2023-11055. The authors would also like to thank the EFFE Industrial Automation R&D Center for their support during the system design stages.

Institutional Review Board Statement: Not applicable.

Informed Consent Statement: Not applicable.

Data Availability Statement: The data that support the findings of this study are available from the corresponding author upon reasonable request.

Conflicts of Interest: The authors declare no conflicts of interest.

References

1. Abidin, A.U.; Munawaroh, A.L.; Rosinta, A.; Sulistiyani, A.T.; Ardianta, I.; Iresha, F.M. Environmental health risks and impacts of PM 2.5 exposure on human health in residential areas, Bantul, Yogyakarta, Indonesia. *Toxicol. Rep.* **2025**, *14*, 101949. https://doi.org/10.1016/j.toxrep.2025.101949.
2. Pope, C.A., 3rd; Dockery, D.W. Health effects of fine particulate air pollution: Lines that connect. *J. Air Waste Manag. Assoc.* **2006**, *56*, 709–742. https://doi.org/10.1080/10473289.2006.10464485.
3. Seinfeld, J.H.; Pandis, S.N. *Atmospheric Chemistry and Physics: From Air Pollution to Climate Change*, 3rd ed.; Wiley: Hoboken, NJ, USA, 2016.
4. Jaworek, A.; Marchewicz, A.; Sobczyk, A.T.; Krupa, A.; Czech, T. Two-stage electrostatic precipitators for the reduction of PM2.5 particle emission. *Prog. Energy Combust. Sci.* **2018**, *67*, 206–233. https://doi.org/10.1016/j.pecs.2018.03.003.
5. Parker, K.R. (Ed.) *Applied Electrostatic Precipitation*; Blackie Academic & Professional: London, UK, 1997.
6. White, H.J. *Industrial Electrostatic Precipitation*; Addison-Wesley Publishing Company: Reading, MA, USA, 1963.
7. Zhao, L.; Dela Cruz, E.I.; Adamiak, K.; Berezin, A.A.; Chang, J.S. A numerical model of a wire–plate electrostatic precipitator under electrohydrodynamic flow conditions. *J. Electrost.* **2006**, *64*, 537–547.
8. Soldati, A. On the effects of electrohydrodynamic flows and turbulence on aerosol transport and collection in wire-plate electrostatic precipitators. *J. Aerosol Sci.* **2000**, *31*, 293–305. https://doi.org/10.1016/S0021-8502(99)00055-5.
9. Arif, S.; Branken, D.J.; Everson, R.C.; Neomagus, H.W.J.P.; le Grange, L.A.; Arif, A. CFD modeling of particle charging and collection in electrostatic precipitators. *J. Electrost.* **2016**, *84*, 10–22. https://doi.org/10.1016/j.elstat.2016.08.008.

10. Zhang, J.; Zhang, L. Prediction and Comparative Analysis of the Influence of Magnetic Field Effect on PM2.5 Trapping Efficiency in Electrostatic Precipitator (ESP) under Different Temperatures. *Appl. Sci.* **2023**, *13*, 12714. https://doi.org/10.3390/app132312714.
11. Kılıç, M.; Mutlu, M.; Altun, A.F. Numerical Simulation and Analytical Evaluation of the Collection Efficiency of the Particles in a Gas by the Wire-Plate Electrostatic Precipitators. *Appl. Sci.* **2022**, *12*, 6401. https://doi.org/10.3390/app12136401.
12. Dong, M.; Zhou, F.; Zhang, Y.; Shang, Y.; Li, S. Numerical study on fine-particle charging and transport behaviour in electrostatic precipitators. *Powder Technol.* **2018**, *330*, 210–218. https://doi.org/10.1016/J.POWTEC.2018.02.038.
13. Park, J.-W.; Kim, C.; Park, J.; Hwang, J. Computational Fluid Dynamic Modelling of Particle Charging and Collection in a Wire-to-Plate Type Single-Stage Electrostatic Precipitator. *Aerosol Air Qual. Res.* **2018**, *18*, 590–601. https://doi.org/10.4209/aaqr.2017.05.0176.
14. Dong, M.; Zhou, F.; Shang, Y.; Li, S. Numerical study on electrohydrodynamic flow and fine-particle collection efficiency in a spike electrode-plate electrostatic precipitator. *Powder Technol.* **2019**, *351*, 71–83. https://doi.org/10.1016/J.POWTEC.2019.03.046.
15. Yang, Z.; Li, H.; Li, Q.; Lin, R.; Jiang, Y.; Yang, Y.; Zheng, C.; Sun, D.; Gao, X. Correlations between Particle Collection Behaviors and Electrohydrodynamics Flow Characteristics in Electrostatic Precipitators. *Aerosol Air Qual. Res.* **2020**, *20*, 2901–2910. https://doi.org/10.4209/aaqr.2020.07.0475.
16. Yang, D.; Guo, B.; Ye, X.; Yu, A.; Guo, J. Numerical simulation of electrostatic precipitator considering the dust particle space charge. *Powder Technol.* **2019**, *354*, 552–560. https://doi.org/10.1016/J.POWTEC.2019.06.013.
17. Skodras, G.; Kaldis, S.P.; Sofialidis, D.; Faltsi, O.; Grammelis, P.; Sakellaropoulos, G.P. Particulate removal via electrostatic precipitators—CFD simulation. *Fuel Process. Technol.* **2006**, *87*, 623–631. https://doi.org/10.1016/j.fuproc.2006.01.012.
18. Zhu, Y.; Gao, M.; Chen, M.; Shi, J.; Shangguan, W. Numerical simulation of capture process of fine particles in electrostatic precipitators under consideration of electrohydrodynamics flow. *Powder Technol.* **2019**, *354*, 653–675. https://doi.org/10.1016/j.powtec.2019.06.038.
19. Choi, H.Y.; Park, Y.G.; Ha, M.Y. Numerical simulation of the wavy collecting plate effects on the performance of an electrostatic precipitator. *Powder Technol.* **2021**, *382*, 232–243. https://doi.org/10.1016/j.powtec.2020.12.070.
20. Zhu, Y.; Chen, C.; Shi, J.; Shangguan, W. Enhancement of air purification by unique W-plate structure in two-stage electrostatic precipitator: A novel design for efficient capture of fine particles. *Adv. Powder Technol.* **2020**, *31*, 1643–1658. https://doi.org/10.1016/J.APT.2020.02.003.
21. Li, J.; Duan, L.; Chen, J.; Li, D.; Bao, S.; Wang, Z.; Wang, J.; Liao, J. Research of the effect of different corrugated dust collection plates on particle removal in electrostatic precipitators. *Chem. Eng. Res. Des.* **2023**, *197*, 323–333. https://doi.org/10.1016/j.cherd.2023.07.006.
22. Nejma, C.; Ben Abdelmlek, K.; Ben Nejma, F. Numerical study on the efficiency of an electrostatic precipitator having the shape of a truncated cone. *Adv. Mech. Eng.* **2024**, *16*, 16878132241272211. https://doi.org/10.1177/16878132241272211.
23. Adamiak, K. Numerical models in simulating wire-plate electrostatic precipitators: A review. *J. Electrost.* **2013**, *71*, 673–680. https://doi.org/10.1016/j.elstat.2013.03.001.
24. Mizuno, A. Electrostatic precipitation. *IEEE Trans. Dielectr. Electr. Insul.* **2000**, *7*, 615–624. https://doi.org/10.1109/94.879357.
25. Jaworek, A.; Adamiak, K. Recent progress in research on electrostatic precipitation (invited paper). *J. Electrost.* **2025**, *137*, 104064. https://doi.org/10.1016/j.elstat.2025.104064.
26. Hu, J.; Wen, J.; Li, H.; Duan, W.; Fan, S.; Xiao, H.; Chen, S. Experiment and numerical simulation on the fine particle migration behaviors for the collection efficiency enhancement of a wire-plate electrostatic precipitator in pig house. *Comput. Electron. Agric.* **2022**, *199*, 107145. https://doi.org/10.1016/J.COMPAG.2022.107145.
27. Ulaby, F.T.; Michielssen, E.; Ravaioli, U. *Fundamentals of Applied Electromagnetics*; Pearson: Boston, MA, USA, 2010.
28. Jaworek, A.; Krupa, A.; Czech, T. Modern electrostatic devices and methods for exhaust gas cleaning: A brief review. *J. Electrost.* **2007**, *65*, 133–155. https://doi.org/10.1016/J.ELSTAT.2006.07.012.
29. Yamamoto, T.; Morita, Y.; Fujishima, H.; Okubo, M. Three-dimensional EHD simulation for point corona electrostatic precipitator based on laminar and turbulent models. *J. Electrost.* **2006**, *64*, 628–633. https://doi.org/10.1016/j.elstat.2005.10.015.
30. Liu, W.K.; Liu, Y.; Farrell, D.; Zhang, L.; Wang, X.S.; Fukui, Y.; Patankar, N.; Zhang, Y.; Bajaj, C.; Lee, J.; et al. Immersed finite element method and its applications to biological systems. *Comput. Methods Appl. Mech. Eng.* **2006**, *195*, 1722–1749. https://doi.org/10.1016/j.cma.2005.05.049.
31. Marin, M.; Hobiny, A.; Abbas, I. Finite Element Analysis of Nonlinear Bioheat Model in Skin Tissue Due to External Thermal Sources. *Mathematics* **2021**, *9*, 1459. https://doi.org/10.3390/math9131459.

32. Markovic, Z.; Eric, M.; Stefanovic, P.; Jovanovic, R.; Lazovic, I. Optimization of the flue gas-flow controlling devices of the electrostatic precipitator of unit A4 in TPP "Nikola Tesla". *Therm. Sci.* **2023**, *27*, 3591–3606. https://doi.org/10.2298/tsci220903024m.
33. Abdykadyrov, A.; Tuleshov, A.; Smailov, N.; Dosbayev, Z.; Marxuly, S.; Sarsenbayev, Y.; Muratbekuly, B.; Kystaubayev, N. Development and Modeling of an Advanced Power Supply System for Electrostatic Precipitators to Improve Environmental Efficiency. *Designs* **2026**, *10*, 34.
34. Ning, Z.; Podlinski, J.; Shen, X.; Li, S.; Wang, S.; Han, P.; Yan, K. Electrode geometry optimization in wire-plate electrostatic precipitator and its impact on collection efficiency. *J. Electrost.* **2016**, *80*, 76–84. https://doi.org/10.1016/j.elstat.2016.02.001.
35. Hu, L.; Pan, C.; Hu, D.; Yan, H.; Qiu, F.; Cheng, Z. Coupled CFD-machine learning optimization of inlet water-jet orifices in jet impact negative pressure reactors. *J. Taiwan Inst. Chem. Eng.* **2025**, *175*, 106248. https://doi.org/10.1016/j.jtice.2025.106248.